Laboratory measurement of the brighter-fatter effect in an H2RG infrared detector

A. A. Plazas[†a], C. Shapiro[a], R. Smith[b], E. Huff[a], & J. Rhodes[a,c,d]

[†]`plazas@caltech.edu`

[a]*Jet Propulsion Laboratory, California Institute of Technology, 4800 Oak Grove Dr., Pasadena, CA 91109, USA*

[b]*Caltech Optical Observatories, 1200 E. California Blvd, CA 91125, USA*

[c]*California Institute of Technology, 1200 E. California Blvd., CA 91125, USA*

[d]*Institute for the Physics and Mathematics of the Universe, 5-1-5 Kashiwanoha, Kashiwa, Chiba Prefecture 277-8583, Japan*

Abstract

The "brighter-fatter" (BF) effect is a phenomenon—originally discovered in charge coupled devices—in which the size of the detector point spread function (PSF) increases with brightness. We present, for the first time, laboratory measurements demonstrating the existence of the effect in a Hawaii-2RG HgCdTe near-infrared (NIR) detector. We use JPL's Precision Projector Laboratory, a facility for emulating astronomical observations with UV/VIS/NIR detectors, to project about 17,000 point sources onto the detector to stimulate the effect. After calibrating the detector for nonlinearity with flat-fields, we find evidence that charge is nonlinearly shifted from bright pixels to neighboring pixels during exposures of point sources, consistent with the existence of a BF-type effect. NASA's Wide Field Infrared Survey Telescope (WFIRST) will use similar detectors to measure weak gravitational lensing from the shapes of hundreds of million of galaxies in the NIR. The WFIRST PSF size must be calibrated to $\approx 0.1\%$ to avoid biased inferences of dark matter and dark energy parameters; therefore further study and calibration of the BF effect in realistic images will be crucial.

1. Introduction

Weak gravitational lensing (WL) of the large-scale matter distribution of the Universe has been identified as one of the main techniques to probe the nature of dark matter and dark energy (Albrecht et al. 2006; Hoekstra and Jain 2008; Kilbinger 2015). Images of distant sources are subtly distorted and magnified by the dark matter distribution along the line of sight. This "cosmic shear" signal has been measured by past and current ground-based galaxy surveys to constrain the current standard cosmological model (DES Collaboration et al. 2017; Troxel et al. 2017; Kuijken et al. 2015). In the future, projects such as the Large Synoptic Survey Telescope (LSST) (Ivezic et al. 2008), ESA's

arXiv:1712.06642v1 [astro-ph.IM] 18 Dec 2017

Euclid spacecraft (Laureijs et al. 2011), and NASA's Wide Field Infrared Telescope Survey (WFIRST) space mission (Spergel et al. 2015) will measure the shapes of hundreds of millions of galaxies to use WL as a cosmic probe.

However, the signal induced by cosmic shear is small (1–2% distortion) and must be measured to a fraction of percent to produce cosmological constraints with the precision required by galaxy surveys. As a consequence, great effort has been placed to understand and characterize the systematic errors that arise during the galaxy shape measurement process. These errors may arise from different sources, e.g., the atmosphere, the telescope optics, galaxy shape measurements, correction for the Point Spread Function (PSF) of the system, redshift distributions, intrinsic alignments of galaxy shapes due to tidal fields, instrumental signatures on the data, etc. (Mandelbaum 2017; Zuntz et al. 2017; Jarvis 2014; Mandelbaum 2015; Stubbs 2014)

WL surveys typically use Charged Coupled Devices (CCDs) in their focal planes. One of the subtle systematic errors that originate in CCDs is known as the "brighter-fatter" effect (BF). This is a nonlinear effect initially measured as a deviation from the linearity in the photon transfer curve of flat field exposures (signal variance as a function of mean signal level), indicating a departure from Poissonian statistics (Downing et al. 2006). The effect also manifests as an increase in the size of point sources—such as stars— with flux (hence the name), due to the deflection of new charges induced by the electric field generated by previously accumulated charge in a given pixel.

The BF effect has been observed in the CCD's of several wide-field cameras such as the Dark Energy Camera (DECam, Flaugher et al. (2015); Gruen et al. (2015)), Megacam (Guyonnet et al. 2015), the Hyper Suprime-Cam (Mandelbaum et al. 2017), and in the prototype sensors of future projects such as LSST and Euclid (Baumer and Roodman 2015; Lage et al. 2017; Niemi et al. 2015). It has been measured to be linear in flux, slightly asymmetric in the channel and serial register directions, achromatic, and long range (e.g., up to 10 pixels in DECam, Gruen et al. (2015)). The BF effect breaks the assumption in astronomical image analysis that the apparent sizes of stars are independent of their brightnesses. Since bright stars are used to determine the PSF, the measured PSF will be systematically larger than the correct PSF that is convolved with the faint galaxies used for WL analyses, inducing shear calibration errors. Mandelbaum (2015) calculate that a 1% mis-estimation in the PSF size caused by the BF effect will induce a multiplicative shear error of ~ 0.02–0.06. Likewise, a 1% ellipticity error will result in an additive term of about 3×10^{-4}. In addition, Huterer et al. (2006) show that—for a spaced-based mission— a multiplicative error of ~ 0.04 will result in a 60% degradation in the marginalized error of the dark energy equation-of-state parameter w_0. Consequently, Stage IV dark energy surveys (as defined by Albrecht et al. (2006)) demand a knowledge of the relative PSF size and ellipticity better than 10^{-3} (Amara and Réfrégier 2008; Paulin-Henriksson et al. 2008, 2009; Cropper et al. 2013; Massey et al. 2013; Spergel et al. 2013).

One way to mitigate the BF effect is to exclude the brightest stars from the shape measurement pipeline (e.g., Jarvis et al. (2015); Zuntz et al. (2017)); however, this is not an ideal solution. Antilogus et al. (2014) have developed a phenomenological model in which the boundaries[1] of a particular pixel shift by an amount proportional to the charge

---

[1]The pixel boundaries in an astronomical detector do not refer to a physical barrier, but are determined

already stored in that pixel and its neighbors. The parameters of the model can be derived from measuring correlations in flat-field images and by assuming certain symmetries in the problem. The model has been shown to be consistent with data from different types of CCDs (Guyonnet et al. 2015), and has been implemented by Gruen et al. (2015) in the publicly available GalSim code (Rowe et al. 2015). In the case of the Hyper Suprime-Cam survey, Mandelbaum et al. (2017) apply a correction that assumes that the electric field transverse to the main drift field can be expressed as the gradient of a potential proportional to the accumulated charge, and demonstrate that the BF-effect is attenuated below scientific requirements.

The future space mission WFIRST will use near-infrared (NIR) detectors, which have a different architecture compared to CCDs and which have not yet been used to perform galaxy shape measurements at the required accuracy for WL science. In particular, the Wide Field Imager of WFIRST will use an array of 18 H4RG-10[2] (with a pixel pitch of 10 μm and a size of 4096 pixels on each side) hybrid complementary metal-oxid-semiconductor (CMOS) devices manufactured by Teledyne (Beletic et al. 2008). Unlike the semiconductor material used in CCDs, the light detecting part of these detectors consists of HgCdTe (mercury cadmium telluride). Photo-generated charges are collected in the depletion region generated at the p-n junction at the detector layer, inducing a change in voltage that is read through non-destructive Fowler sampling or "up-the-ramp" sampling. The detector layer is connected to a readout integration circuit layer, which transmits the charge to off-chip electronics for digitization.

While the BF effect is well-known in CCDs, it has not been studied in detail in NIR detectors. Despite their physical differences with CCDs, Plazas et al. (2017) (P17 hereafter) propose that there are physical motivations to expect a BF effect in CMOS NIR detectors. As charge accumulates in a particular pixel, the depletion region shrinks. Depending on the signal contrast between adjacent pixels, new charge generated close to the midpoint between pixel centers will have higher probability of being collected in the pixel with a larger depletion region area. This effect depends on the signal contrast between adjacent pixels. P17 use archival images of the globular cluster Omega centauri (Ω-cen)—obtained with the infrared H1RG-18 device of the Wide Field Camera 3 (WFC3-IR) on the Hubble Space Telescope—to look for the BF effect. By analyzing the central 3×3 region of bright (but unsaturated) stars, P17 find evidence for charge redistribution from the central pixel to neighboring pixels as the integration time increases.[3]

In this work we use data from Precision Projector Laboratory (PPL) (Shapiro et al. 2017; Seshadri et al. 2013; Shapiro et al. 2013) to study the BF effect in NIR detectors, extending the initial analysis performed in P17. The PPL is a facility run by NASA's Jet Propulsion Laboratory (operated by the California Institute of Technology) with support from Caltech Optical Observatories (COO). It was designed to assess the impact of detector effects on space-based astronomical observations such as weak lensing shape measurements.

---

by electric fields that define a plane that indicates by which pixel a charge will be captured.

[2]HAWAII—HgCdTe Astronomical Wide Area Infrared Imager—Reference pixels and Guide mode.

[3]P17 follows an analysis by Jay Anderson (STScI), who presented preliminary results on the BF effect with the same type of data (Ω-cen images taken with the WFC3-IR channel) at a WFIRST meeting in May of 2016.

Laboratory measurements provide several advantages over on-sky data, which suffer from effects such as drift, thermal instability, and source confusion. Tests at the PPL can be repeated numerous times under controlled conditions, allowing us to achieve a more reliable measurement. The PPL test-bed ("the projector") is stable and versatile, with a wide range of control of the flux, wavelength, position, and f-number of the projected images. Images (e.g., a grid of point sources) can be focused with high Strehl ratio over the entire area of a detector, which provides a multiplexed advantage over e.g. scanning a single bright spot.

This paper is organized as follows: in Section 2 we describe the laboratory setup and parameters, as well as the characteristics of the NIR detector used to acquire the data analyzed. In Section 3 we summarize the PPL data calibration and analysis steps, including correction for known effects such as nonlinearity in the conversion from charge to voltage (known as "voltage nonlinearity" or "classical nonlinearity"—NL;Hilbert (2014, 2008); Plazas et al. (2016)) and electronic coupling between pixels (known as "inter pixel capacitance"—IPC; Hilbert and McCullough (2011); McCullough (2008)). We also present null tests that validate our measurement pipeline using simulations. Results are shown in Section 4. Finally, we conclude in Section 5.
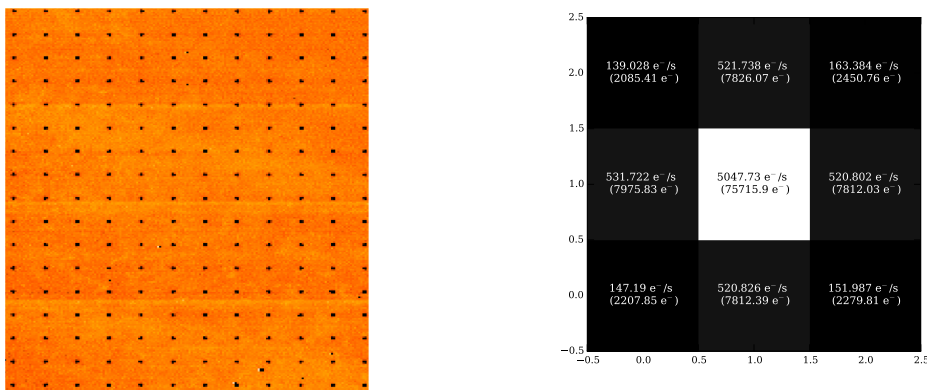

Fig. 1.— *Left*: Subsection of a grid of ~ 17000 point sources projected on a 2k×2k H2RG detector at the PPL. *Right*: Postage stamp showing the inner 3×3 pixels region of the PPL spots, obtained by taking the median over approximately 700 sources with a centroid < 0.1 pixels away from the pixel center. Each point in the grid is strongly under-sampled (FWHM < 1 pixel).

2. Data and simulations

2.1. Precision Projector Laboratory Data

The detector tested in this experiment was an engineering-grade Teledyne H2RG-18 NIR detector (2048^2 pixels; 18 μm pitch) with a cutoff wavelength of 2.3 μm. The NIR detector working group for the Euclid mission lent the H2RG to the PPL for the purpose of investigating intra-pixel response variations, which impact the photometric accuracy of the Near Infrared Spectrophotometer (NISP; Maciaszek et al. (2016); Prieto et al. (2012)). That study will be presented in a separate paper. The H2RG (SN 18546) is designated engineering-grade primarily due to a large collection of inoperable pixels in one

corner. It is otherwise an unexceptional device, and we presume that the BF effect results presented here will be qualitatively representative of other HxRG devices, in particular the H4RG-10 detectors planned for the WFIRST imaging survey. Conventional performance characterization of the H2RG was conducted by Teledyne before transfer of the device to the PPL.

We use the PPL test-bed to project a grid of approximately 17000 point sources ("stars" or "spots") on the H2RG with a uniform spacing of 274.5 μm (15.25 pixels), illuminated by a broadband quartz-tungsten-halogen lamp with Y-band filter (0.9–1.07 μm). Setting the focal ratio to f/11 produces a diffraction limited PSF with a full-width-half-maximum (FWHM) of about 11 μm, broadened to about 14 μm (0.78 pixels) by lateral charge diffusion and seeing. The PSF flux is thus strongly concentrated within the area of a single pixel. Fig. 1 shows an image of the spot grid on a subregion of the detector and a typical (median) flux distribution of the central 3×3 pixels when a spot is centered on a pixel.

The detector was operated at a temperature of 95 K with a room-temperature Leach controller clocked at 166 kHz. In 32-channel readout mode, the maximum frame-rate is about 1.2 Hz for the full detector area, but in practice we sampled at 0.33 Hz to avoid a data writing glitch (which has since been fixed). Fluxes are measured by "sampling up the ramp", i.e. non-destructively reading each pixel at regular (3 s) intervals during an exposure. For each ramp, we discard the first frame sampled immediately after resetting to mitigate transient effects caused by the reset. Thus with 6 frames per ramp and a total exposure time of 15 seconds, we analyze the final 5 frames (12 s). We apply a mean conversion gain of 2.7 e$^-$/ADU and measure a median read noise of 15 e$^-$ (correlated-double-sampling noise for 2 consecutive frames).

For calibration purposes, dark frames (which include thermal background and light leakage) and flat-field images (uniform illumination) are taken with the same frame-rate and exposure time as the spot images. Our data set consists of 100 spots and flat-field ramps, and 10 dark-frames ramps. Under the illumination conditions, the average central pixel of a spot reaches $\sim$ 76000 e$^-$ in an exposure (about 5000 e$^-$/s) while for the flat-field images it reaches $\sim$ 95500 e$^-$(about 6400 e$^-$/s) after correcting for NL. These correspond to 57% (spots) and 72% (flats) of the 132245 e$^-$ mean well depth (defined by onset of 4% NL; measured by Teledyne). With a mean background level of 94 e$^-$/s/pixel, the exposures are shot noise dominated with a signal-to noise ratio (SNR) of about 120 per frame for the central pixel of a spot.

2.2. Simulations

We also simulate exposures that resemble the lab data in order to asses the performance of our measurement pipeline and characterize its response to different parameters. We use the code GalSim[4] (v. 1.3.0) to create 90 spots ramps with a grid of 1024 point sources on a 2k by 2k pixels image, using an empirical PSF model that matches the diffraction-limited PSF of our experimental setup. We use this grid of spots as input for a simulator that produces ramps that have the same number of frames and integration time

---

[4]https://github.com/GalSim-developers/GalSim

of the laboratory data (6 and 15 seconds, respectively). We also generate 90 flat and dark ramps. The simulator includes the option of applying different sources of noise such as shot noise and readout noise (set to 15 e$^-$ r.m.s.), IPC, classical nonlinearity (NL), and the BF effect model (Antilogus et al. 2014; Gruen et al. 2015) built-in in GalSim.[5]

3. Methods

As in P17, we record the inner 3×3 pixel region (a "postage stamp") of each spot in order to look for evidence of the BF effect in the PPL data. An advantage of non-destructive reads is that we can compare the fluxes in each spot at the end of an exposure to flux at the beginning, instead of comparing different spots (which adds PSF noise) or different exposures (which adds shot noise). We look for deviations from constant flux after correcting for known effects such as NL and IPC. We calibrate the NL per pixel by using flat-field images, where we expect the contribution to nonlinearity in the signal due to the BF effect to be suppressed, given that the signal contrast between pixels is small for a mean flat-field image. After correcting NL in the spot images, we look for evidence of non-constant flux due to the charge contrast between pixels.

We discard the first 10 ramps of the initial set of 100 spot and flat-field ramps to mitigate the impact of the "burn-in" effect, an effect—different from persistence (Smith and Rahmer 2008; Biesiadzinski et al. 2011)—in which the sensitivity of the detector to light is increased following previous exposures.[6] In addition, we have visually inspected the ramps formed by taking the mean of a region of size 1800×1800 pixels in each frame for the dark, flat, and spot exposure types, and have discarded additional outliers ramps. The remaining number of ramps is thus 9, 85, and 84 for the darks, flats, and spots, respectively.

We then calculate the median ramp of each set in order to increase the SNR. In addition to improvements in SNR, stacking the ramps averages over lamp fluctuations[7] and other systematic errors such as image motion and seeing (Shapiro et al. (2017) show that the mean position across the detector has a displacement of about 1 μm r.m.s. for a single image.). We run SExtractor (Bertin 2006) on the sample with the longest integration time of the median spots ramps, using a mask flagging bad pixels produced with laboratory measurements. In this way, we identify the approximate location of the spots in our images, and calculate the unweighted centroid from the inner 3×3 postage stamp of each spot. We initially select those sources with a centroid within $\pm$ 0.1 pixels of the pixel center to maximize the signal contrast (and thereby increasing the BF amplitude) between the central pixel of each spot and its nearest neighbors. We assume that IPC does not change with time and that it is spatially uniform, and correct for it by applying the following kernel, measured at the PPL comparing the signal in hot pixels and that in their adjacent

---

[5] galsim.cdmodel

[6] This effect has been observed in H4RG-10 data taken at the Detector Characterization Laboratory in Goddard's Space Flight Center.

[7] Previous photometry experiments at the PPL have demonstrated stability in the brightness of point sources to the level of 1 part in 10^4 over observing series of hours (Touli et al. 2014).
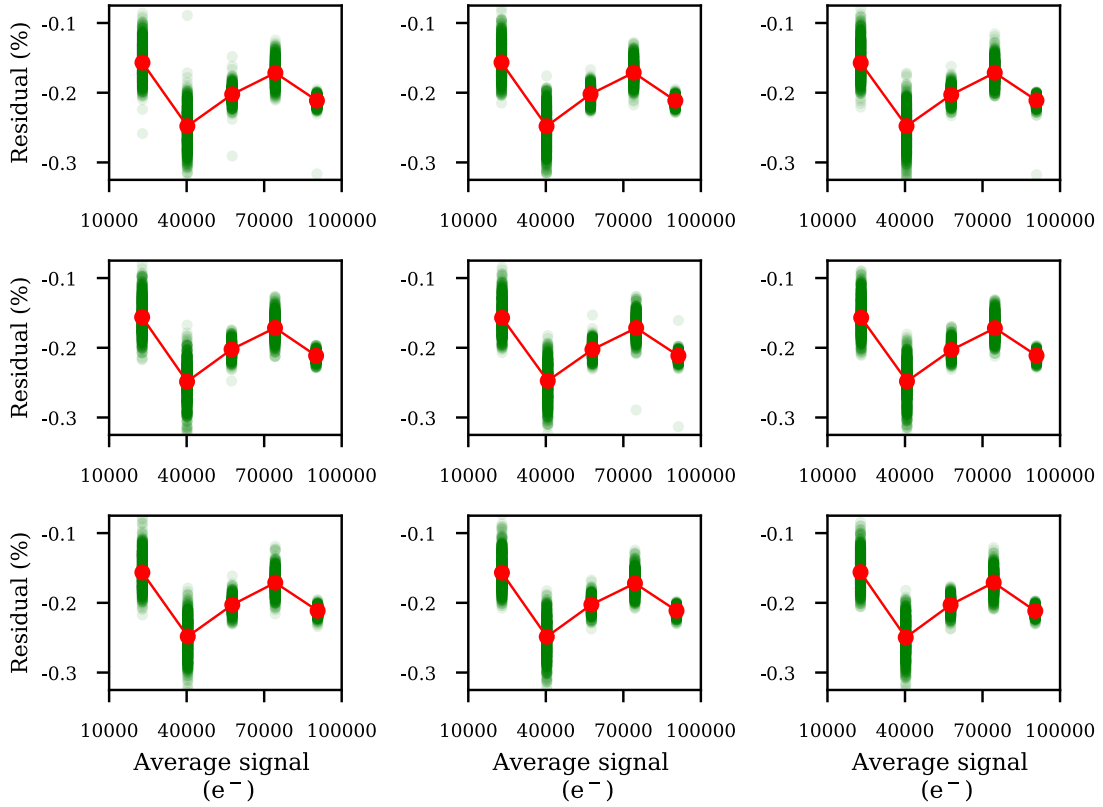
Fig. 2.— Fractional NL residuals in flat-field images. The pixel positions of the center of the spots are used in the stacked flat-field image to select 748 3×3 pixels regions (a postage stamp) around that center. Then, the signal—before dark subtraction—in each of the 9 pixels of each region is fitted to Eqn. 2, and the relative residuals per frame are reported in the y-axis (green spots). The x-axis shows the mean signal averaged over the 9 pixels of each region. The red line represents the median value per frame.

neighbors (Hilbert and McCullough 2011; McCullough 2008):

$$K = \begin{pmatrix} 0 & -0.007 & 0 \\ -0.009 & 0.968 & -0.009 \\ 0 & -0.007 & 0 \end{pmatrix} \quad (1)$$

Under the assumption of linear IPC, the impact of IPC can be distinguished from the BF-effect since the former redistributes a fixed fraction of a pixel signal to its neighbors while the latter is contrast-dependent. We convert the ADU numbers from raw images to electrons by using an IPC-corrected average mean of 2.7 $e^-/$ADU. We then fit a quadratic polynomial to the signal ramp in each pixel, $S(e^-)$, in order to correct for classical voltage nonlinearity:

$$S = C_0 + C_1 t + C_2(C_1 t)^2 \quad (2)$$

In Eq. 2, C_0 represents an offset in the ramp due to a reset voltage, and $C_1 t \equiv Q_L(t)$ is the linear flux component of the signal. P17 show (their Appendix A) that the dependence on capacitance of voltage in the pixel diode leads to an approximate quadratic response at low to medium signals. Figure 2 shows that this quadratic polynomial model correctly describes flat-fielded data to 0.1% (on average), up to a signal level of approximately 95000 e^- (72% of the mean full-well of the pixels of the detector).

In terms of the parameters of the fit, the corrected signal $Q_L(t)$ (the signal that would have been detected by a linear detector) is given by solving the quadratic formula as in Kubik et al. (2014):

$$Q_L(t) = \frac{1}{2C_0}(-1 + \sqrt{1 - 4C_2(C_0 - S)}) \quad (3)$$

We use the quadratic coefficient C_2 fitted from the flat-field images to correct the spot and dark ramps for NL. After subtracting the corrected dark signal from the corrected spot signal for each pixel in the 3×3 postage stamp, we convert the signal in each pixel ramp (in e^-) into a flux rate (in $1/e^-$ per seconds). Finally, to quantify post-calibration nonlinearity when switching from flat-field images to spot images—an indicator of the BF effect—we define the relative flux deviation in a pixel as follows:

$$f_N(k) = \frac{F_k - F_1}{F_*} \quad (4)$$

where F_k is the pixel flux calculated by differencing the kth and $(k+1)$th frames (the discarded reset frame is $k = 0$), and F_* is the time-averaged total flux of the 9 central pixels of the spot. Eqn. 4 differs from the metric used in P17 by the normalization F_*, which in this case is defined as:

$$F_* = \frac{\sum_p (S_{p,M-1} - S_{p,1})}{\Delta t(M - 2)} \quad (5)$$

where $S_{p,k}$ is the signal in the kth frame of the pth pixel, $M = 6$ is the total number of frames, and $\Delta t = 3$ s is the frame time. The sum is over the 9 central pixels.

4. Results

4.1. Measurement of flux deviations in point source images

We quantify post-calibration nonlinearity in the stacked spot image by measuring $f_N(k)$ for each pixel in the 3×3 postage stamp around each spot, for each frame k. We

select spots with centroids within 0.1 pixels of a pixel center to maximize the charge contrast between the central pixel and its nearest neighbors. We then calculate the average over the spots of the signal $f_N(k)$, after rejecting outliers through 3σ clipping. The final number of spots that satisfy these conditions is 748, and the results are shown in Fig. 3 as a function of the average (over the 748 spots) of the mean integrated signal between the consecutive frames that define F_k (the mean fluence of the $(k+1)$th and kth frames). As the exposures integrate, f_N in the central pixel decreases, meaning its flux is lower

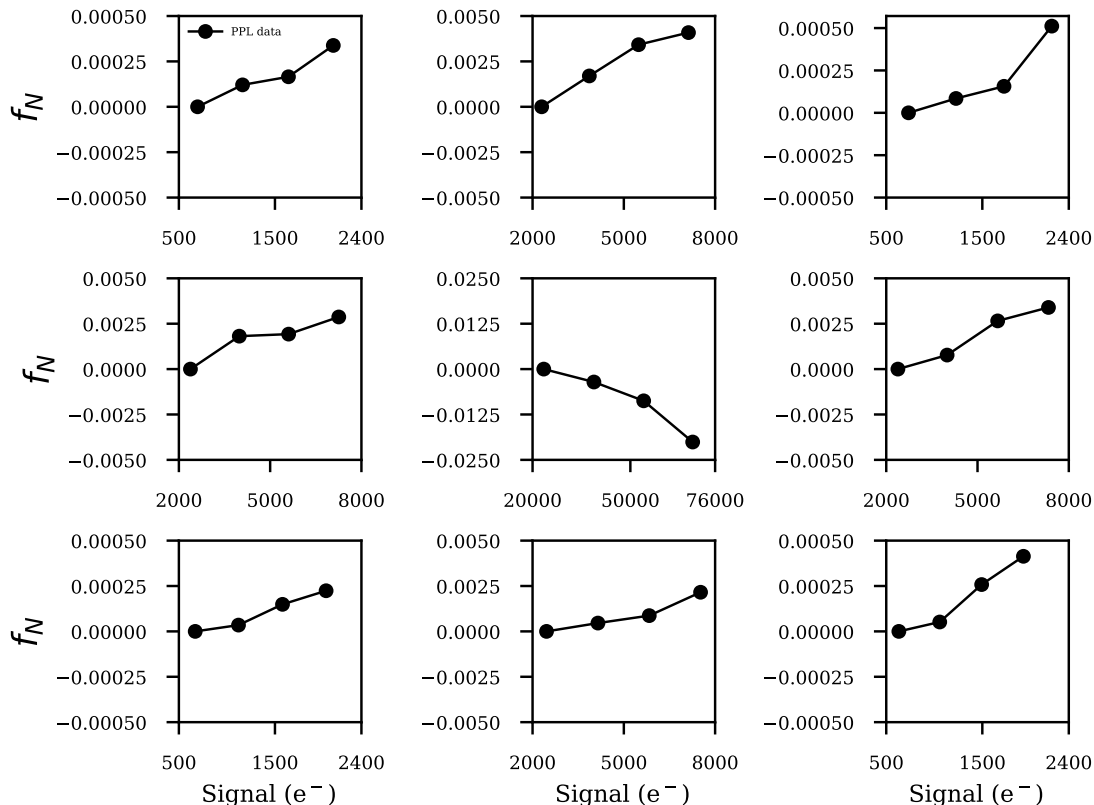Fig. 3.— For each pixel in a 3×3 region containing a spot, we plot the average f_N – the change in flux relative to the start of the exposure, normalized by the average total flux of the spot. The data is averaged over 84 exposures and over 748 spots with a centroid < 0.1 pixels away from a pixel center. f_N is plotted as a function of the mean integrated signal between the two consecutive frames from which flux is estimated. The error bars, which are computed from the standard error of the mean taken over all spots, are smaller than the symbols.

relative to the beginning of the exposures by up to 2.1% of the total spot flux. This is accompanied by a simultaneous increase in the four nearest neighboring pixels, as would be expected from the shifting of effective pixel boundaries induced by a BF-type effect. As shown in Fig. 4, the excess flux in the eight outer pixels of the stamp is comparable to the flux loss in the central pixel; therefore, charge conservation in this region is nearly but not perfectly satisfied. As a check on our analysis pipeline, Fig. 5 shows the f_N values obtained when using simulated data (90 spots and flat ramps, each one with an initial grid of 1024 centered spots; 841 points remaining after analyzing the images with our measurement pipeline, which included rejection of sections of the detector where bad pixels lie in the
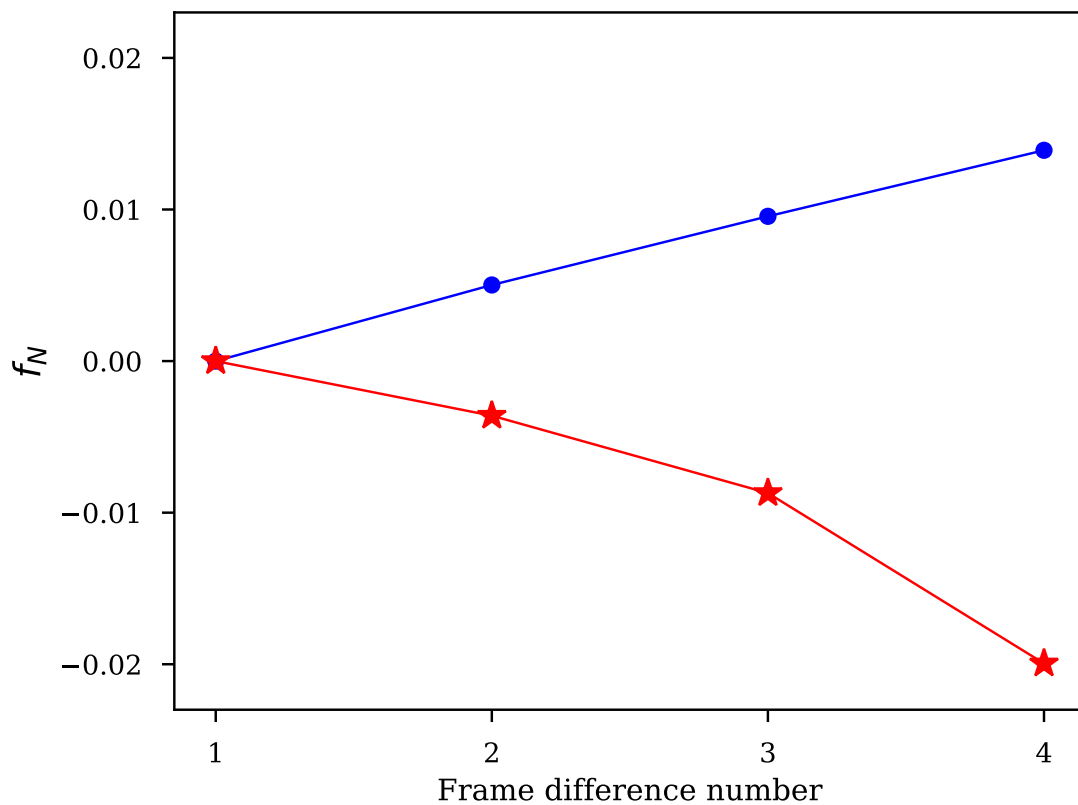
Fig. 4.— The upper line (blue, circles) represents the sum of the f_N signal in each of the outer 8 pixels in Fig. 3. The lower line (red, stars) is the f_N signal in the central pixel of Fig. 3. The similar amplitude (with opposite sign) indicates that charge is for the most part conserved (just redistributed) withing the 3×3 postage stamp. The scale of the y-axis is the same as that of the central pixel in Fig. 3.

actual lab data). The baseline case with noiseless images (and no IPC, NL, or BF effect) is consistent with a null result (red, solid line in Fig. 5). We then add noise and NL to the
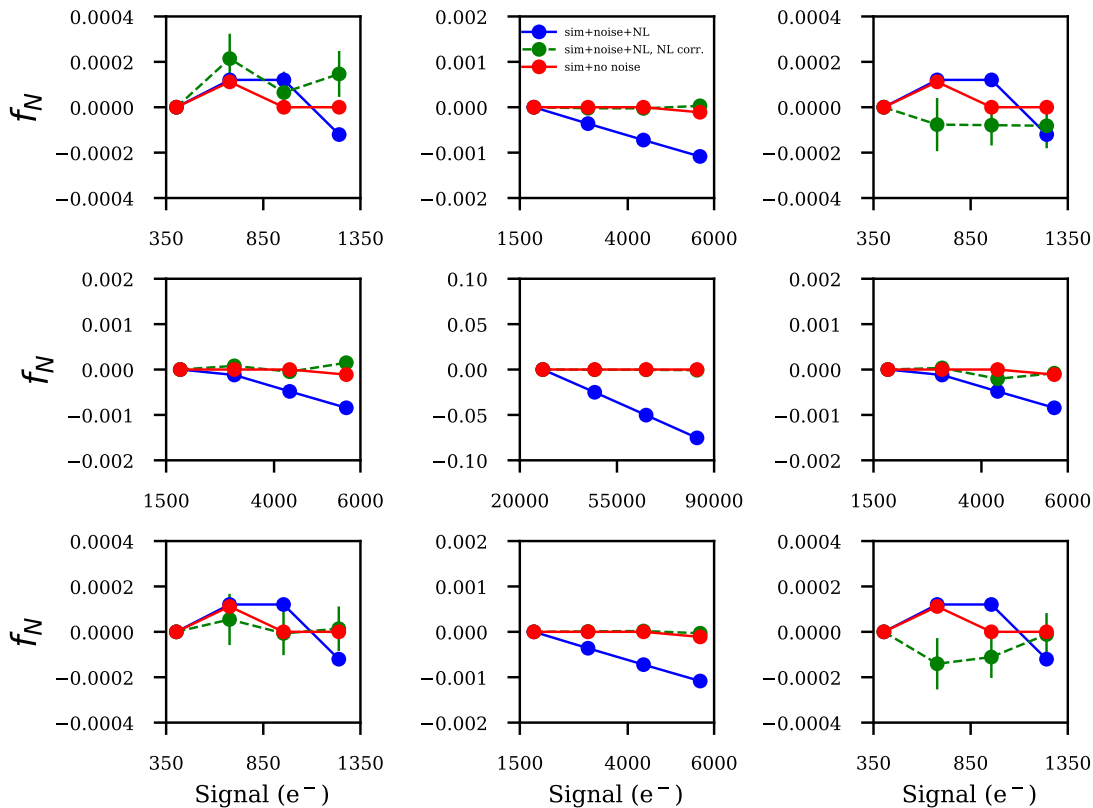

Fig. 5.— Same as Fig. 3, but using simulations of centered spots (841 out of 1024 initial spots) instead of PPL data. Blue solid line: simulations with shot and read noise and classical NL applied (but not corrected), where C_2 follows a distribution of the form $\mathcal{N} \sim (-7.76 \times 10^{-6}, 0.36 \times 10^{-7})$. Green dashed line: same as blue, but with NL corrected with Eqn. 3 as described in the text.

simulations, with NL applied in the form of a polynomial quadratic in the charge:

$$Q(e) \rightarrow Q - \beta Q^2, \tag{6}$$

with a second-order coefficient amplitude β drawn from a Normal distribution of the form $\mathcal{N} \sim (-7.76 \times 10^{-7}, \ 0.36 \times 10^{-7})$, consistent with measurements of NL on flat-field images at the laboratory. IPC is also applied (as given by Eqn.1), and subsequently deconvolved by the analysis pipeline, as would be done with actual data.. If the effect of NL is not corrected by using Eqn. 3, the f_N metric decreases as a function of time, with its amplitude being larger for the central pixel that concentrates more charge (Fig. 5, blue solid line). When the correction is applied, the results are consistent with a null value for f_N (Fig. 5, green dashed line).

Notice that the effect of NL on f_N has the same, negative sign as integration time increases in each pixel (i.e., there is a decrease in the charge recorded, as expected), whereas in the case of the results with the PPL spots, the sign of the effect is opposite between the central pixel and its four nearest neighbors, as expected from charge redistribution caused by a BF-type effect.
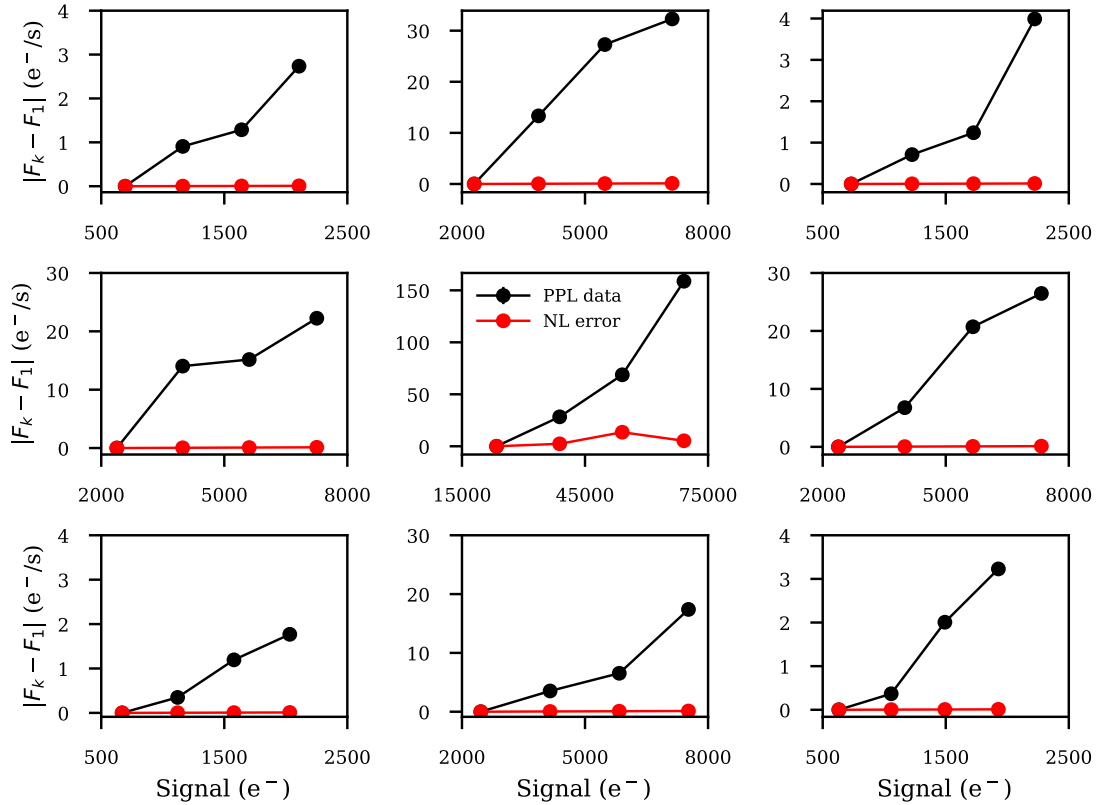
Fig. 6.— Absolute value of flux changes per pixel relative to the beginning of a spot exposure. Black points use the same spot data as in Fig. 3 while red points show the estimated error due to the residuals of the NL model. Flux F_k is estimated from the differences between frames $k + 1$ and k, and the x-axis is given by the average fluence between those frames. We do not use the reset frame ($k = 0$). The NL error was estimated by modulating a simulated signal of the average spot in Fig: 1 with the NL residual functions shown in Fig. 2.

Since we are inferring the BF effect from changes in flux during an exposure, we must demonstrate that the residuals of our quadratic NL model are not the source of the observed flux changes. To assess the impact of the residuals, we first simulate a median spot using the fluxes shown in Fig. 1. We then modulate each ramp from each pixel of the average spot with the NL residual functions from Fig. 2 to obtain the absolute fluence error expected from the NL residuals. The residuals are linearly interpolated and extrapolated to low fluences by defining them to be zero at zero fluence. We compute the change in flux induced between frames $F_k - F_1$ (i.e., the numerator of Eqn. 4) by the fluence errors, and compare them to the corresponding quantities measured from the PPL data (c.f., Fig. 3). The results in Fig: 6 show the detected flux changes, which range from a few e^-/s in the corner pixels to 160 e^-/s in the center, are significantly larger than the expected errors due to insufficient calibration of NL.
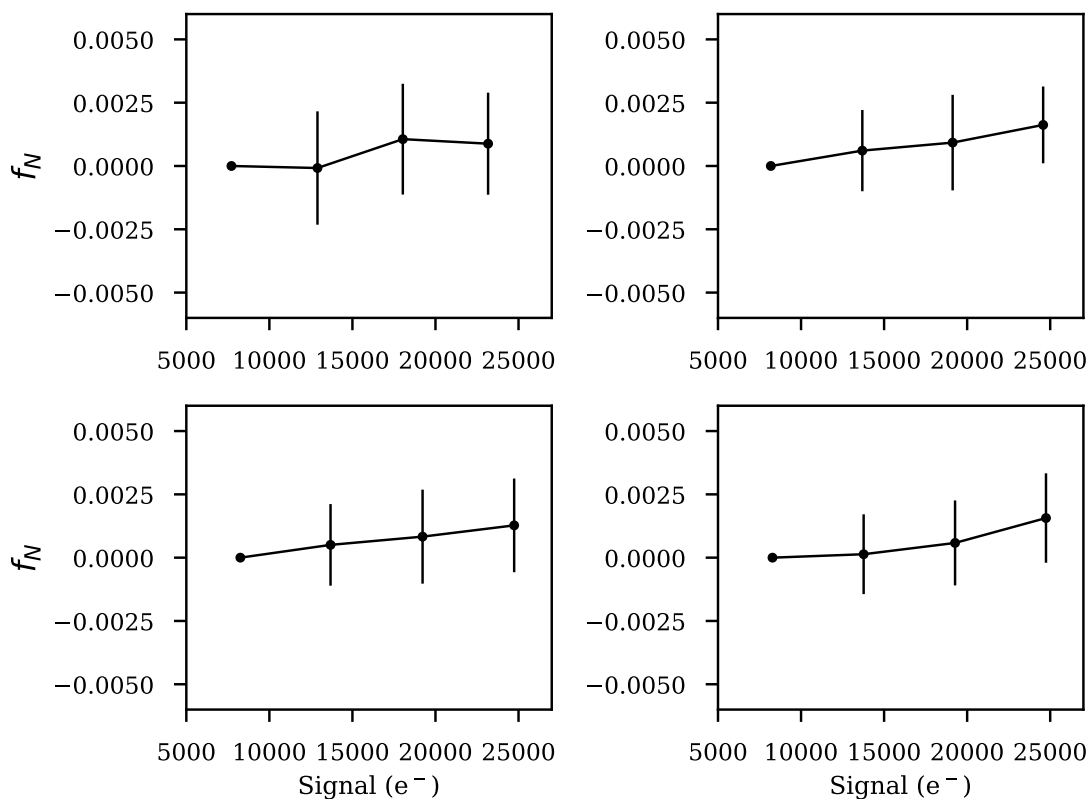

Fig. 7.— f_N as a function of mean frame signal for PPL spots whose centroid lies within 0.1 pixels of the pixel corner (as opposed to the pixel center, c.f. Fig. 3). The charge is approximately evenly distributed among 4 pixels because the centroid is close to one of the four corners of the central pixel in the 3×3 pixels region. For each case, we isolated the 4 pixels that contain the majority of the signal, and produced a stacked imaged by taking the mean of each of these four 2×2 pixels subregions (i.e., translating them onto each other). The f_N metric from this stacked image is shown here.The number of spots for each of the four cases is 40, 50, 43, and 50, respectively. Notice that the scale of the y-axis is the same as that of the 4 nearest neighbors of the central pixel in Fig. 3.

As a check on whether the BF effect depends on the signal contrast between adjacent pixels, we repeat our analysis on spots whose centroids are within 0.1 pixels of a pixel

corner (with the charge approximately evenly distributed among four pixels), expecting an attenuation of the signal. Fig. 7 shows the f_N metric results for this particular case. As expected, the fluxes in each pixel are more constant (no change detected) during the exposures despite the spots having similar total fluxes to spots centered on a pixel.
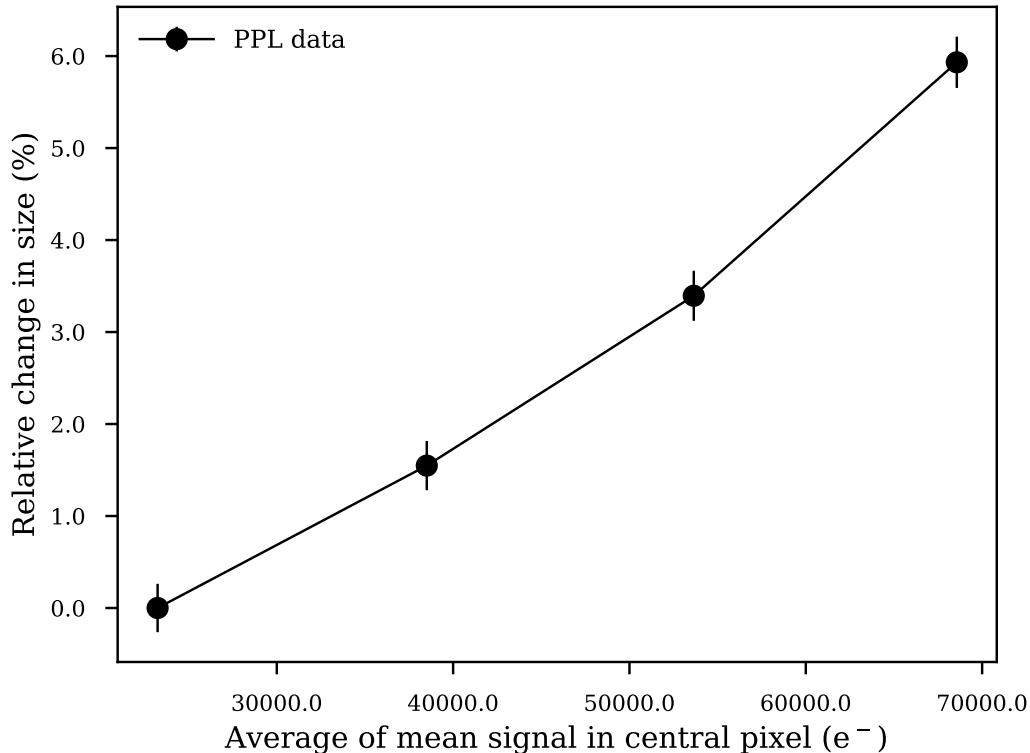

Fig. 8.— Average relative change in size (second moment of the 3×3 postage stamp) of the projected spots as a function of the average (over all the spots) of the mean signal in the central pixel between consecutive frames. The size is measured in the postage stamp formed by the difference of two consecutive frames, with the first difference being used as reference. The error bars represent the standard error of the mean value.

We also calculate the increase in the average relative size of the spots as the ramp is sampled in time. For the stamp formed as the difference between consecutive frames of a given ramp, we calculate the size r, defined as a linear combination of the second moments of the postage stamp I weighted by a Gaussian of $\sigma = 1$ pixel:

$$r = M_{11} + M_{22} \tag{7}$$

$$M_{k,l} = \frac{\sum_{i,j} x_{k,l} I_{i,j} w_{i,j}}{\sum_{i,j} I_{i,j} w_{i,j}}$$

Fig. 8 shows the normalized size (average over spots) with respect to the first frame difference (i.e., $r_k/r_1 - 1$) as a function of the average (over all the spots) of the mean signal in the central pixel between consecutive frames, for the same PPL spots as in Fig. 3. We detect a linear relative increase in the size of approximately 6% as integration time increases (c.f. with the 0.1% or 10^{-3} maximum change in relative change in size demanded by WL science in WFIRST).

4.2. Estimating change in pixel area

Assuming that the measured postcalibration nonlinearity is entirely due to an effective change in size of the central pixel in a spot (ignoring other possible NL contributions such as nonlinear IPC), and assuming that the change in pixel area is proportional to charge contrast with nearest neighbor pixels, we can model the effect on flux in the central bright pixel as:

$$\frac{dQ}{dt} = F(t) = F_0\left(1 + BQ_c(t)\right) = F_0\left(1 + BF_c t\right), \tag{8}$$

where F_0 represents the unmodified flux in the pixel (in e^-/s), and Q_c and F_c are the mean charge and flux contrast between the central pixel and its four nearest neighbors, respectively:

$$Q_c = Q_{central} - (Q_{left} + Q_{right} + Q_{top} + Q_{bottom})/4 \tag{9}$$
$$Q_c = F_c t$$

For simplicity, we model the change in flux as being proportional to F_0, but more accurately, it would depend on the value of the spot profiles at the pixel boundaries being shifted. The mean F_c is approximately constant, assuming that it is large compared to the amplitude of the BF effect. The proportionality constant B quantifies the area change (dA/A) per e^- of contrast Q_c (thus, the units of B are $1/e^-$). We calculate B by fitting the measured f_N in the central pixel of each spot to a linear function of the form $f_N = mk$ (for frame number k being). Setting F_0 to the flux in the first frame (F_1) and $t \equiv k\Delta t$ in Eqn. 8, f_N (Eqn. 4) can be rewritten as:

$$f_N = \frac{BF_1 F_c \Delta t}{F_*} k \tag{10}$$

Thus, the constant B can be calculated using the slope from the linear fit as:

$$B = \frac{m}{F_c}\left(\frac{F_*}{F_1 \Delta t}\right) \tag{11}$$

Fig. 9 shows the distribution of B coefficients as calculated for 748 spots that satisfied the centroid condition (<0.1 pixels from a pixel center). The scatter of the distribution has contributions from random noise (dominated by shot noise), systematic errors, and the intrinsic scatter of the B coefficient itself. To assess the contribution from shot noise, we have simulated 90 ramps with shot noise and perfectly centered spots on a 2k by 2k grid, using the Antilogus et al. (2014) model in `GalSim` to simulate the BF effect corresponding to a single value of B.[8] The resulting distribution of B from the simulations is shown in Fig. 9 as well (green), and it shows that the scatter in the measured B parameter (red) is not entirely due to noise but also has contribution from intrinsic scatter in B or systematic errors, including possible errors in our model. The measured mean of the B distribution is -0.41±0.0076 ppm/e^- (the negative sign indicating shrinkage of the central pixel). This provides an initial order of magnitude estimate of the BF effect, which can be refined by more in-depth treatment of systematics, and which may of course depend on the particular device and its operating conditions.

---

[8]The parameters of the `GalSim` model for the BF effect were chosen to resemble the measured mean: `galsim.cdmodel.PowerLawCD (1, 1.1e-7, 1.1e-7, 1.0e-7, 1.0e-7, 0.0, 0.0, 0.0)`. The exact meaning of each parameter can be found in the `Galsim` documentation.
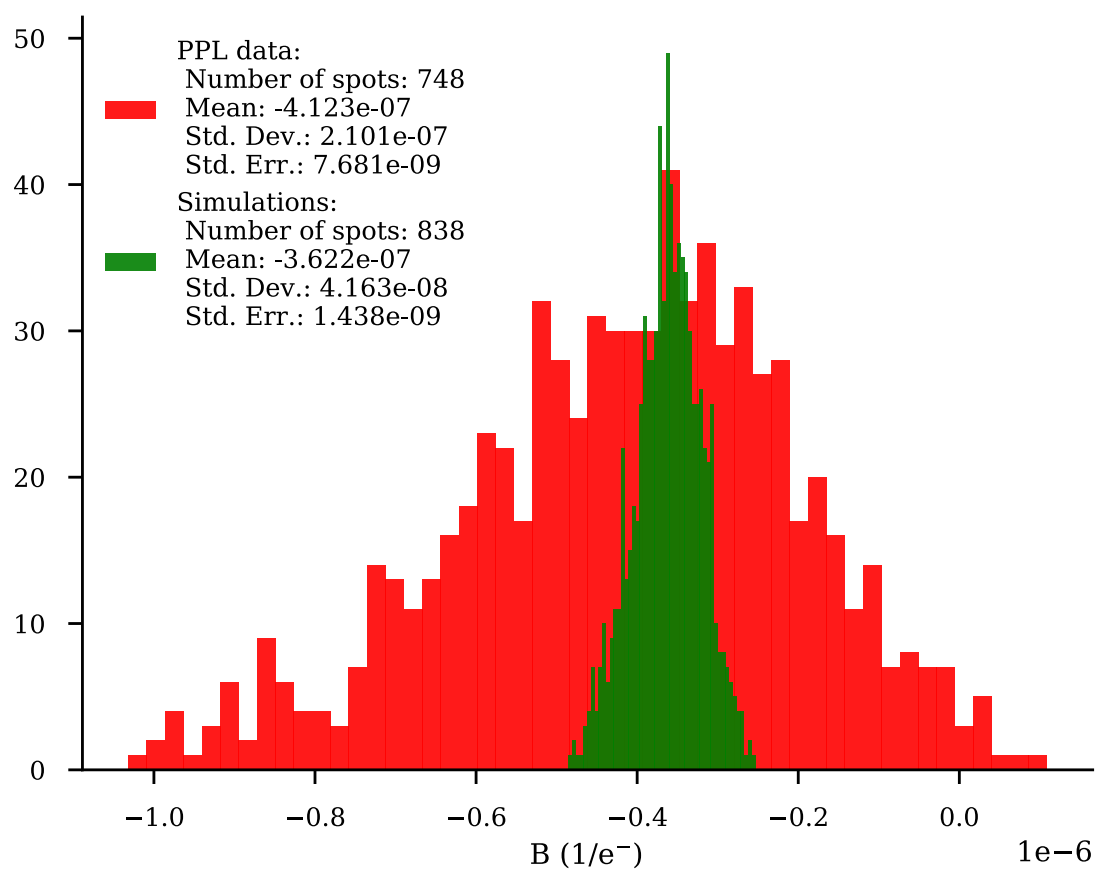
Fig. 9.— Histogram of B coefficient as defined in Eqn. 11: PPL data (red) and simulations with noise, NL, and BF effect applied (green).

5. Conclusions

We have directly demonstrated the existence of a BF effect in an H2RG-18 NIR detector by studying exposures of compact point sources generated at JPL's Precision Projector Laboratory. Using a stable and controlled laboratory environment, we extend and confirm the analysis in Plazas et al. (2017) (initiated by J. Anderson, Space Telescope Science Institute), which found preliminary evidence for a BF-type effect in Hubble/WFC3-IR data. We find evidence of charge redistribution from the central pixel of a bright point source to neighboring pixels after correcting for known effects such as classical voltage nonlinearity and linear IPC (assumed to be spatially uniform). Using 1 μm illumination and spots with FWHM=0.78 pixels, we measure a relative increase in the average spot size of about 5% once the central bright pixel reaches 76000 e$^-$ (57% of the mean pixel well depth). Our results are consistent with the physical concept proposed in Plazas et al. (2017), that the shrinking of the depletion region in each pixel diode causes a contrast-dependent shift in the effective pixel boundaries. Assuming this mechanism, our measurements can be interpreted as a shrinking of the central bright pixel of the spot image, approximately parameterized as a 0.41 ± 0.0076 ppm reduction in area per electron of charge contrast with neighbor pixels.

If not corrected, the BF effect induces PSF shape measurement errors that will significantly degrade galaxy shape measurements in WL science analyses using HxRG detectors, such as WFIRST which requires PSF sizes measured to 0.1%. Shifting pixel boundaries may also cause photometric and astrometric errors in NIR supernova and microlensing measurements, especially in crowded fields where measurements may be influenced by nearby bright sources. Future work should further characterize and model the effect, exploring dependence on parameters such as illumination wavelength, integration time, and source size/shape. Sensitivity to detector bias voltages should also be studied to understand the physics of the effect. Of course we expect the BF effect to be device-dependent: the results here are not fully applicable to the H4RG-10 detectors (10 μm pitch) planned for the WFIRST Wide Field Instrument, but they are likely to be qualitatively similar. It will be crucial for WFIRST and other astronomy missions using HxRG detectors (e.g. James Webb Space Telescope and the Thirty Meter Telescope) to not only characterize the BF effect but also to validate that precision measurements (shapes, astrometry, and photometry) can be recovered after applying an intended correction scheme on representative devices. The PPL detector emulation facility is well-suited for studies of this type thanks to the speed, stability, and versatility of the projector testbed.

out at the Jet Propulsion Laboratory, California Institute of Technology, under a contract with the National Aeronautics and Space Administration.

REFERENCES

A. Albrecht, G. Bernstein, R. Cahn, W. L. Freedman, J. Hewitt, W. Hu, J. Huth, M. Kamionkowski, E. W. Kolb, L. Knox, J. C. Mather, S. Staggs, and N. B. Suntzeff. Report of the Dark Energy Task Force. *ArXiv Astrophysics e-prints*, September 2006.

A. Amara and A. Réfrégier. Systematic bias in cosmic shear: extending the Fisher matrix. *MNRAS*, 391:228–236, November 2008. doi: 10.1111/j.1365-2966.2008.13880.x.

P. Antilogus, P. Astier, P. Doherty, A. Guyonnet, and N. Regnault. The brighter-fatter effect and pixel correlations in CCD sensors. *Journal of Instrumentation*, 9:C03048, March 2014. doi: 10.1088/1748-0221/9/03/C03048.

M. A. Baumer and A. Roodman. Intrinsic pixel size variation in an LSST prototype sensor. *Journal of Instrumentation*, 10:C05024, May 2015. doi: 10.1088/1748-0221/10/05/C05024.

James W. Beletic, Richard Blank, David Gulbransen, Donald Lee, Markus Loose, Eric C. Piquette, Thomas Sprafke, William E. Tennant, Majid Zandian, and Joseph Zino. Teledyne imaging sensors: infrared imaging technologies for astronomy and civil space, 2008.

E. Bertin. Automatic Astrometric and Photometric Calibration with SCAMP. In C. Gabriel, C. Arviset, D. Ponz, and S. Enrique, editors, *Astronomical Data Analysis Software and Systems XV*, volume 351 of *Astronomical Society of the Pacific Conference Series*, page 112, July 2006.

T. Biesiadzinski, W. Lorenzon, R. Newman, M. Schubnell, G. Tarlé, and C. Weaverdyck. Measurement of Reciprocity Failure in Near-Infrared Detectors. *PASP*, 123:179–186, February 2011. doi: 10.1086/658282.

M. Cropper, H. Hoekstra, T. Kitching, R. Massey, J. Amiaux, L. Miller, Y. Mellier, J. Rhodes, B. Rowe, S. Pires, C. Saxton, and R. Scaramella. Defining a weak lensing experiment in space. *MNRAS*, 431:3103–3126, June 2013. doi: 10.1093/mnras/stt384.

DES Collaboration, T. M. C. Abbott, F. B. Abdalla, A. Alarcon, J. Aleksić, S. Allam, S. Allen, A. Amara, J. Annis, J. Asorey, S. Avila, D. Bacon, E. Balbinot, M. Banerji, N. Banik, W. Barkhouse, M. Baumer, E. Baxter, K. Bechtol, M. R. Becker, A. Benoit-Lévy, B. A. Benson, G. M. Bernstein, E. Bertin, J. Blazek, S. L. Bridle, D. Brooks, D. Brout, E. Buckley-Geer, D. L. Burke, M. T. Busha, D. Capozzi, A. Carnero Rosell, M. Carrasco Kind, J. Carretero, F. J. Castander, R. Cawthon, C. Chang, N. Chen, M. Childress, A. Choi, C. Conselice, R. Crittenden, M. Crocce, C. E. Cunha, C. B. D'Andrea, L. N. da Costa, R. Das, T. M.

Davis, C. Davis, J. De Vicente, D. L. DePoy, J. DeRose, S. Desai, H. T. Diehl, J. P. Dietrich, S. Dodelson, P. Doel, A. Drlica-Wagner, T. F. Eifler, A. E. Elliott, F. Elsner, J. Elvin-Poole, J. Estrada, A. E. Evrard, Y. Fang, E. Fernandez, A. Ferté, D. A. Finley, B. Flaugher, P. Fosalba, O. Friedrich, J. Frieman, J. García-Bellido, M. Garcia-Fernandez, M. Gatti, E. Gaztanaga, D. W. Gerdes, T. Giannantonio, M. S. S. Gill, K. Glazebrook, D. A. Goldstein, D. Gruen, R. A. Gruendl, J. Gschwend, G. Gutierrez, S. Hamilton, W. G. Hartley, S. R. Hinton, K. Honscheid, B. Hoyle, D. Huterer, B. Jain, D. J. James, M. Jarvis, T. Jeltema, M. D. Johnson, M. W. G. Johnson, T. Kacprzak, S. Kent, A. G. Kim, A. King, D. Kirk, N. Kokron, A. Kovacs, E. Krause, C. Krawiec, A. Kremin, K. Kuehn, S. Kuhlmann, N. Kuropatkin, F. Lacasa, O. Lahav, T. S. Li, A. R. Liddle, C. Lidman, M. Lima, H. Lin, N. MacCrann, M. A. G. Maia, M. Makler, M. Manera, M. March, J. L. Marshall, P. Martini, R. G. McMahon, P. Melchior, F. Menanteau, R. Miquel, V. Miranda, D. Mudd, J. Muir, A. Möller, E. Neilsen, R. C. Nichol, B. Nord, P. Nugent, R. L. C. Ogando, A. Palmese, J. Peacock, H. V. Peiris, J. Peoples, W. J. Percival, D. Petravick, A. A. Plazas, A. Porredon, J. Prat, A. Pujol, M. M. Rau, A. Refregier, P. M. Ricker, N. Roe, R. P. Rollins, A. K. Romer, A. Roodman, R. Rosenfeld, A. J. Ross, E. Rozo, E. S. Rykoff, M. Sako, A. I. Salvador, S. Samuroff, C. Sánchez, E. Sanchez, B. Santiago, V. Scarpine, R. Schindler, D. Scolnic, L. F. Secco, S. Serrano, I. Sevilla-Noarbe, E. Sheldon, R. C. Smith, M. Smith, J. Smith, M. Soares-Santos, F. Sobreira, E. Suchyta, G. Tarle, D. Thomas, M. A. Troxel, D. L. Tucker, B. E. Tucker, S. A. Uddin, T. N. Varga, P. Vielzeuf, V. Vikram, A. K. Vivas, A. R. Walker, M. Wang, R. H. Wechsler, J. Weller, W. Wester, R. C. Wolf, B. Yanny, F. Yuan, A. Zenteno, B. Zhang, Y. Zhang, and J. Zuntz. Dark Energy Survey Year 1 Results: Cosmological Constraints from Galaxy Clustering and Weak Lensing. *ArXiv e-prints*, August 2017.

M. Downing, D. Baade, P. Sinclaire, S. Deiries, and F. Christen. CCD riddle: a) signal vs time: linear; b) signal vs variance: non-linear. In *Society of Photo-Optical Instrumentation Engineers (SPIE) Conference Series*, volume 6276 of *Proc. SPIE*, page 627609, June 2006. doi: 10.1117/12.671457.

B. Flaugher, H. T. Diehl, K. Honscheid, T. M. C. Abbott, O. Alvarez, R. Angstadt, J. T. Annis, M. Antonik, O. Ballester, L. Beaufore, G. M. Bernstein, R. A. Bernstein, B. Bigelow, M. Bonati, D. Boprie, D. Brooks, E. J. Buckley-Geer, J. Campa, L. Cardiel-Sas, F. J. Castander, J. Castilla, H. Cease, J. M. Cela-Ruiz, S. Chappa, E. Chi, C. Cooper, L. N. da Costa, E. Dede, G. Derylo, D. L. DePoy, J. de Vicente, P. Doel, A. Drlica-Wagner, J. Eiting, A. E. Elliott, J. Emes, J. Estrada, A. Fausti Neto, D. A. Finley, R. Flores, J. Frieman, D. Gerdes, M. D. Gladders, B. Gregory, G. R. Gutierrez, J. Hao, S. E. Holland, S. Holm, D. Huffman, C. Jackson, D. J. James, M. Jonas, A. Karcher, I. Karliner, S. Kent, R. Kessler, M. Kozlovsky, R. G. Kron, D. Kubik, K. Kuehn, S. Kuhlmann, K. Kuk, O. Lahav, A. Lathrop, J. Lee, M. E. Levi, P. Lewis, T. S. Li, I. Mandrichenko, J. L. Marshall, G. Martinez, K. W. Merritt, R. Miquel, F. Muñoz, E. H. Neilsen, R. C. Nichol, B. Nord, R. Ogando, J. Olsen, N. Palaio, K. Patton, J. Peoples, A. A. Plazas, J. Rauch, K. Reil, J.-P. Rheault, N. A. Roe, H. Rogers, A. Roodman, E. Sanchez, V. Scarpine, R. H. Schindler, R. Schmidt, R. Schmitt, M. Schubnell, K. Schultz, P. Schurter, L. Scott, S. Serrano, T. M. Shaw, R. C. Smith, M. Soares-Santos, A. Stefanik, W. Stuermer,

E. Suchyta, A. Sypniewski, G. Tarle, J. Thaler, R. Tighe, C. Tran, D. Tucker, A. R. Walker, G. Wang, M. Watson, C. Weaverdyck, W. Wester, R. Woods, B. Yanny, and DES Collaboration. The Dark Energy Camera. *AJ*, 150:150, November 2015. doi: 10.1088/0004-6256/150/5/150.

D. Gruen, G. M. Bernstein, M. Jarvis, B. Rowe, V. Vikram, A. A. Plazas, and S. Seitz. Characterization and correction of charge-induced pixel shifts in DECam. *Journal of Instrumentation*, 10:C05032, May 2015. doi: 10.1088/1748-0221/10/05/C05032.

A. Guyonnet, P. Astier, P. Antilogus, N. Regnault, and P. Doherty. Evidence for self-interaction of charge distribution in charge-coupled devices. *A&A*, 575:A41, March 2015. doi: 10.1051/0004-6361/201424897.

B. Hilbert. WFC3 TV3 Testing: IR Channel Nonlinearity Correction. Technical report, 2008.

B. Hilbert. Updated non-linearity calibration method for WFC3/IR. Technical report, July 2014.

B. Hilbert and P. McCullough. Interpixel Capacitance in the IR Channel: Measurements Made On Orbit. Technical report, April 2011.

H. Hoekstra and B. Jain. Weak gravitational lensing and its cosmological applications. *Annual Review of Nuclear and Particle Systems*, 58:99–123, 2008.

D. Huterer, M. Takada, G. Bernstein, and B. Jain. Systematic errors in future weak-lensing surveys: requirements and prospects for self-calibration. *MNRAS*, 366:101–114, February 2006. doi: 10.1111/j.1365-2966.2005.09782.x.

Z. Ivezic, J. A. Tyson, B. Abel, E. Acosta, R. Allsman, Y. AlSayyad, S. F. Anderson, J. Andrew, R. Angel, G. Angeli, R. Ansari, P. Antilogus, K. T. Arndt, P. Astier, E. Aubourg, T. Axelrod, D. J. Bard, J. D. Barr, A. Barrau, J. G. Bartlett, B. J. Bauman, S. Beaumont, A. C. Becker, J. Becla, C. Beldica, S. Bellavia, G. Blanc, R. D. Blandford, J. S. Bloom, J. Bogart, K. Borne, J. F. Bosch, D. Boutigny, W. N. Brandt, M. E. Brown, J. S. Bullock, P. Burchat, D. L. Burke, G. Cagnoli, D. Calabrese, S. Chandrasekharan, S. Chesley, E. C. Cheu, J. Chiang, C. F. Claver, A. J. Connolly, K. H. Cook, A. Cooray, K. R. Covey, C. Cribbs, W. Cui, R. Cutri, G. Daubard, G. Daues, F. Delgado, S. Digel, P. Doherty, R. Dubois, G. P. Dubois-Felsmann, J. Durech, M. Eracleous, H. Ferguson, J. Frank, M. Freemon, E. Gangler, E. Gawiser, J. C. Geary, P. Gee, M. Geha, R. R. Gibson, D. K. Gilmore, T. Glanzman, I. Goodenow, W. J. Gressler, P. Gris, A. Guyonnet, P. A. Hascall, J. Haupt, F. Hernandez, C. Hogan, D. Huang, M. E. Huffer, W. R. Innes, S. H. Jacoby, B. Jain, J. Jee, J. G. Jernigan, D. Jevremovic, K. Johns, R. L. Jones, C. Juramy-Gilles, M. Juric, S. M. Kahn, J. S. Kalirai, N. Kallivayalil, B. Kalmbach, J. P. Kantor, M. M. Kasliwal, R. Kessler, D. Kirkby, L. Knox, I. Kotov, V. L. Krabbendam, S. Krughoff, P. Kubanek, J. Kuczewski, S. Kulkarni, R. Lambert, L. Le Guillou, D. Levine, M. Liang, K. Lim, C. Lintott, R. H. Lupton, A. Mahabal, P. Marshall, S. Marshall, M. May, R. McKercher, M. Migliore, M. Miller, D. J. Mills, D. G. Monet, M. Moniez, D. R. Neill, J. Nief, A. Nomerotski, M. Nordby, P. O'Connor, J. Oliver, S. S. Olivier, K. Olsen, S. Ortiz, R. E. Owen, R. Pain, J. R. Peterson,

C. E. Petry, F. Pierfederici, S. Pietrowicz, R. Pike, P. A. Pinto, R. Plante, S. Plate, P. A. Price, M. Prouza, V. Radeka, J. Rajagopal, A. Rasmussen, N. Regnault, S. T. Ridgway, S. Ritz, W. Rosing, C. Roucelle, M. R. Rumore, S. Russo, A. Saha, B. Sassolas, T. L. Schalk, R. H. Schindler, D. P. Schneider, G. Schumacher, J. Sebag, G. H. Sembroski, L. G. Seppala, I. Shipsey, N. Silvestri, J. A. Smith, R. C. Smith, M. A. Strauss, C. W. Stubbs, D. Sweeney, A. Szalay, P. Takacs, J. J. Thaler, R. Van Berg, D. Vanden Berk, K. Vetter, F. Virieux, B. Xin, L. Walkowicz, C. W. Walter, D. L. Wang, M. Warner, B. Willman, D. Wittman, S. C. Wolff, W. M. Wood-Vasey, P. Yoachim, H. Zhan, and for the LSST Collaboration. LSST: from Science Drivers to Reference Design and Anticipated Data Products. *ArXiv e-prints*, May 2008.

M Jarvis. Challenges for precision shape measurements. *Journal of Instrumentation*, 9 (03):C03017, 2014. URL http://stacks.iop.org/1748-0221/9/i=03/a=C03017.

M. Jarvis, E. Sheldon, J. Zuntz, T. Kacprzak, S. L. Bridle, A. Amara, R. Armstrong, M. R. Becker, G. M. Bernstein, C. Bonnett, C. Chang, R. Das, J. P. Dietrich, A. Drlica-Wagner, T. F. Eifler, C. Gangkofner, D. Gruen, M. Hirsch, E. M. Huff, B. Jain, S. Kent, D. Kirk, N. MacCrann, P. Melchior, A. A. Plazas, A. Refregier, B. Rowe, E. S. Rykoff, S. Samuroff, C. Sánchez, E. Suchyta, M. A. Troxel, V. Vikram, T. Abbott, F. B. Abdalla, S. Allam, J. Annis, A. Benoit-Lévy, E. Bertin, D. Brooks, E. Buckley-Geer, D. L. Burke, D. Capozzi, A. Carnero Rosell, M. Carrasco Kind, J. Carretero, F. J. Castander, M. Crocce, C. E. Cunha, C. B. D'Andrea, L. N. da Costa, D. L. DePoy, S. Desai, H. T. Diehl, P. Doel, A. Fausti Neto, B. Flaugher, P. Fosalba, J. Frieman, E. Gaztanaga, D. W. Gerdes, R. A. Gruendl, G. Gutierrez, K. Honscheid, D. J. James, K. Kuehn, N. Kuropatkin, O. Lahav, T. S. Li, M. Lima, M. March, P. Martini, R. Miquel, J. J. Mohr, E. Neilsen, B. Nord, R. Ogando, K. Reil, A. K. Romer, A. Roodman, M. Sako, E. Sanchez, V. Scarpine, M. Schubnell, I. Sevilla-Noarbe, R. C. Smith, M. Soares-Santos, F. Sobreira, M. E. C. Swanson, G. Tarle, J. Thaler, D. Thomas, A. R. Walker, and R. H. Wechsler. The DES Science Verification Weak Lensing Shear Catalogs. *ArXiv e-prints*, July 2015.

M. Kilbinger. Cosmology with cosmic shear observations: a review. *Reports on Progress in Physics*, 78(8):086901, July 2015. doi: 10.1088/0034-4885/78/8/086901.

B. Kubik, R. Barbier, A. Castera, E. Chabanat, S. Ferriol, and G. Smadja. Impact of noise covariance and nonlinearities in NIR H2RG detectors. In *High Energy, Optical, and Infrared Detectors for Astronomy VI*, volume 9154 of *Proc. SPIE*, page 91541Q, July 2014. doi: 10.1117/12.2055318.

K. Kuijken, C. Heymans, H. Hildebrandt, R. Nakajima, T. Erben, J. T. A. de Jong, M. Viola, A. Choi, H. Hoekstra, L. Miller, E. van Uitert, A. Amon, C. Blake, M. Brouwer, A. Buddendiek, I. F. Conti, M. Eriksen, A. Grado, J. Harnois-Déraps, E. Helmich, R. Herbonnet, N. Irisarri, T. Kitching, D. Klaes, F. La Barbera, N. Napolitano, M. Radovich, P. Schneider, C. Sifón, G. Sikkema, P. Simon, A. Tudorica, E. Valentijn, G. Verdoes Kleijn, and L. van Waerbeke. Gravitational lensing analysis of the Kilo-Degree Survey. *MNRAS*, 454:3500–3532, December 2015. doi: 10.1093/mnras/stv2140.

C. Lage, A. Bradshaw, and J. A. Tyson. Measurements and simulations of the brighter-

fatter effect in CCD sensors. *Journal of Instrumentation*, 12:C03091, March 2017. doi: 10.1088/1748-0221/12/03/C03091.

R. Laureijs, J. Amiaux, S. Arduini, J. . Auguères, J. Brinchmann, R. Cole, M. Cropper, C. Dabin, L. Duvet, A. Ealet, and et al. Euclid Definition Study Report. *ArXiv e-prints*, October 2011.

T. Maciaszek, A. Ealet, K. Jahnke, E. Prieto, R. Barbier, Y. Mellier, F. Beaumont, W. Bon, A. Bonnefoi, M. Carle, A. Caillat, A. Costille, D. Dormoy, F. Ducret, C. Fabron, A. Febvre, B. Foulon, J. Garcia, J.-L. Gimenez, E. Grassi, P. Laurent, D. Le Mignant, L. Martin, C. Rossin, T. Pamplona, P. Sanchez, S. Vives, J. C. Clémens, W. Gillard, M. Niclas, A. Secroun, B. Serra, B. Kubik, S. Ferriol, J. Amiaux, J. C. Barrière, M. Berthe, C. Rosset, J. F. Macias-Perez, N. Auricchio, A. De Rosa, E. Franceschi, G. P. Guizzo, G. Morgante, F. Sortino, M. Trifoglio, L. Valenziano, L. Patrizii, T. Chiarusi, F. Fornari, F. Giacomini, A. Margiotta, N. Mauri, L. Pasqualini, G. Sirri, M. Spurio, M. Tenti, R. Travaglini, S. Dusini, F. Dal Corso, F. Laudisio, C. Sirignano, L. Stanco, S. Ventura, E. Borsato, C. Bonoli, F. Bortoletto, A. Balestra, M. D'Alessandro, E. Medinaceli, R. Farinelli, L. Corcione, S. Ligori, F. Grupp, C. Wimmer, F. Hormuth, G. Seidel, S. Wachter, C. Padilla, M. Lamensans, R. Casas, I. Lloro, R. Toledo-Moreo, J. Gomez, C. Colodro-Conde, D. Lizán, J. J. Diaz, P. B. Lilje, C. Toulouse-Aastrup, M. I. Andersen, A. N. Sørensen, P. Jakobsen, A. Hornstrup, N.-C. Jessen, C. Thizy, W. Holmes, U. Israelsson, M. Seiffert, A. Waczynski, R. J. Laureijs, G. Racca, J.-C. Salvignol, T. Boenke, and P. Strada. Euclid Near Infrared Spectrometer and Photometer instrument concept and first test results obtained for different breadboards models at the end of phase C. In *Space Telescopes and Instrumentation 2016: Optical, Infrared, and Millimeter Wave*, volume 9904 of *Proc. SPIE*, page 99040T, July 2016. doi: 10.1117/12.2232941.

R. Mandelbaum. Instrumental systematics and weak gravitational lensing. *Journal of Instrumentation*, 10(05):C05017, 2015. URL http://stacks.iop.org/1748-0221/10/i=05/a=C05017.

R. Mandelbaum. Weak lensing for precision cosmology. *ArXiv e-prints*, October 2017.

R. Mandelbaum, H. Miyatake, T. Hamana, M. Oguri, M. Simet, R. Armstrong, J. Bosch, R. Murata, F. Lanusse, A. Leauthaud, J. Coupon, S. More, M. Takada, S. Miyazaki, J. S. Speagle, M. Shirasaki, C. Sifón, S. Huang, A. J. Nishizawa, E. Medezinski, Y. Okura, N. Okabe, N. Czakon, R. Takahashi, W. Coulton, C. Hikage, Y. Komiyama, R. H. Lupton, M. A. Strauss, M. Tanaka, and Y. Utsumi. The first-year shear catalog of the Subaru Hyper Suprime-Cam SSP Survey. *ArXiv e-prints*, May 2017.

R. Massey, H. Hoekstra, T. Kitching, J. Rhodes, M. Cropper, J. Amiaux, D. Harvey, Y. Mellier, M. Meneghetti, L. Miller, S. Paulin-Henriksson, S. Pires, R. Scaramella, and T. Schrabback. Origins of weak lensing systematics, and requirements on future instrumentation (or knowledge of instrumentation). *MNRAS*, 429:661–678, February 2013. doi: 10.1093/mnras/sts371.

P. McCullough. Inter-pixel capacitance: prospects for deconvolution. Technical report, August 2008.

S.-M. Niemi, M. Cropper, M. Szafraniec, and T. Kitching. Measuring a charge-coupled device point spread function. Euclid visible instrument CCD273-84 PSF performance. *Experimental Astronomy*, 39:207–231, June 2015. doi: 10.1007/s10686-015-9440-7.

S. Paulin-Henriksson, A. Amara, L. Voigt, A. Refregier, and S. L. Bridle. Point spread function calibration requirements for dark energy from cosmic shear. *A&A*, 484: 67–77, June 2008. doi: 10.1051/0004-6361:20079150.

S. Paulin-Henriksson, A. Refregier, and A. Amara. Optimal point spread function modeling for weak lensing: complexity and sparsity. *A&A*, 500:647–655, June 2009. doi: 10.1051/0004-6361/200811061.

A. A. Plazas, C. Shapiro, J. Rhodes, R. Mandelbaum, R. Smith, and A. Kannawadi. The effect of detector nonlinearity on WFIRST PSF profiles for weak gravitational lensing measurements. *Publications of the Astronomical Society of the Pacific, Volume 128, Number 968,(2016)*, 2016.

A. A. Plazas, C. Shapiro, R. Smith, J. Rhodes, and E. Huff. Nonlinearity and pixel shifting effects in HXRG infrared detectors. *Journal of Instrumentation*, 12:C04009, April 2017. doi: 10.1088/1748-0221/12/04/C04009.

E. Prieto, J. Amiaux, J.-L. Auguères, J. C. Barrière, C. Bonoli, F. Bortoletto, C. Cerna, L. Corcione, L. Duvet, A. Ealet, B. Garilli, P. Gondoin, F. Grupp, K. Jahnke, R. J. Laureijs, S. Ligori, O. Le Fèvre, T. Maciaszek, F. Madrid, J. Martignac, L. Martin, G. Morgante, Y. Mellier, T. Pamplona, R. Holmes, R. Grange, M. Riva, C. Rossin, G. Seidel, G. Smadja, R. Toledo-Moreo, M. Trifoglio, L. Valenziano, and F. Zerbi. Euclid near-infrared spectrophotometer instrument concept at the end of the phase A study. In *Space Telescopes and Instrumentation 2012: Optical, Infrared, and Millimeter Wave*, volume 8442 of *Proc. SPIE*, page 84420W, September 2012. doi: 10.1117/12.926265.

B. T. P. Rowe, M. Jarvis, R. Mandelbaum, G. M. Bernstein, J. Bosch, M. Simet, J. E. Meyers, T. Kacprzak, R. Nakajima, J. Zuntz, H. Miyatake, J. P. Dietrich, R. Armstrong, P. Melchior, and M. S. S. Gill. GALSIM: The modular galaxy image simulation toolkit. *Astronomy and Computing*, 10:121–150, April 2015. doi: 10.1016/j.ascom.2015.02.002.

S. Seshadri, C. Shapiro, T. Goodsall, J. Fucik, C. Hirata, J. D. Rhodes, B. T. P. Rowe, and R. M. Smith. Initial Results from a Laboratory Emulation of Weak Gravitational Lensing Measurements. *PASP*, 125:1065, September 2013. doi: 10.1086/673318.

C. Shapiro, B. T. P. Rowe, T. Goodsall, C. Hirata, J. Fucik, J. Rhodes, S. Seshadri, and R. Smith. Weak Gravitational Lensing Systematics from Image Combination. *PASP*, 125:1496–1513, December 2013. doi: 10.1086/674415.

C. Shapiro, R. Smith, E. Huff, A. A. Plazas, J. Rhodes, J. Fucik, T. Goodsall, R. Massey, B. Rowe, and S Seshadri. Precision Projector Laboratory: Detector Characterization with an Astronomical Emulation Testbed. In *Paola Amico (ed.), SDW2017 Conference Proceedings*, Proc. SPIE, 2017.

R. Smith and Rahmer. Pixel Area Variations in CCDs and implications for precision photometry. In *SPIE Conference Series*, volume 7021 of *Proc. SPIE*, 2008.

D. Spergel, N. Gehrels, J. Breckinridge, M. Donahue, A. Dressler, B. S. Gaudi, T. Greene, O. Guyon, C. Hirata, J. Kalirai, N. J. Kasdin, W. Moos, S. Perlmutter, M. Postman, B. Rauscher, J. Rhodes, Y. Wang, D. Weinberg, J. Centrella, W. Traub, C. Baltay, J. Colbert, D. Bennett, A. Kiessling, B. Macintosh, J. Merten, M. Mortonson, M. Penny, E. Rozo, D. Savransky, K. Stapelfeldt, Y. Zu, C. Baker, E. Cheng, D. Content, J. Dooley, M. Foote, R. Goullioud, K. Grady, C. Jackson, J. Kruk, M. Levine, M. Melton, C. Peddie, J. Ruffa, and S. Shaklan. Wide-Field InfraRed Survey Telescope-Astrophysics Focused Telescope Assets WFIRST-AFTA Final Report. *ArXiv e-prints*, May 2013.

D. Spergel, N. Gehrels, C. Baltay, D. Bennett, J. Breckinridge, M. Donahue, A. Dressler, B. S. Gaudi, T. Greene, O. Guyon, C. Hirata, J. Kalirai, N. J. Kasdin, B. Macintosh, W. Moos, S. Perlmutter, M. Postman, B. Rauscher, J. Rhodes, Y. Wang, D. Weinberg, D. Benford, M. Hudson, W.-S. Jeong, Y. Mellier, W. Traub, T. Yamada, P. Capak, J. Colbert, D. Masters, M. Penny, D. Savransky, D. Stern, N. Zimmerman, R. Barry, L. Bartusek, K. Carpenter, E. Cheng, D. Content, F. Dekens, R. Demers, K. Grady, C. Jackson, G. Kuan, J. Kruk, M. Melton, B. Nemati, B. Parvin, I. Poberezhskiy, C. Peddie, J. Ruffa, J. K. Wallace, A. Whipple, E. Wollack, and F. Zhao. Wide-Field InfrarRed Survey Telescope-Astrophysics Focused Telescope Assets WFIRST-AFTA 2015 Report. *ArXiv e-prints*, March 2015.

C. W. Stubbs. Precision astronomy with imperfect fully depleted CCDs: an introduction and a suggested lexicon. *Journal of Instrumentation*, 9:C03032, March 2014. doi: 10.1088/1748-0221/9/03/C03032.

D. Touli, C. A. Beichman, G. Vasisht, R. Smith, and J. E. Krist. Emulating JWST Exoplanet Transit Observations in a Testbed laboratory experiment. In J. Ballet, F. Martins, F. Bournaud, R. Monier, and C. Reylé, editors, *SF2A-2014: Proceedings of the Annual meeting of the French Society of Astronomy and Astrophysics*, pages 75–76, December 2014.

M. A. Troxel, N. MacCrann, J. Zuntz, T. F. Eifler, E. Krause, S. Dodelson, D. Gruen, J. Blazek, O. Friedrich, S. Samuroff, J. Prat, L. F. Secco, C. Davis, A. Ferté, J. DeRose, A. Alarcon, A. Amara, E. Baxter, M. R. Becker, G. M. Bernstein, S. L. Bridle, R. Cawthon, C. Chang, A. Choi, J. De Vicente, A. Drlica-Wagner, J. Elvin-Poole, J. Frieman, M. Gatti, W. G. Hartley, K. Honscheid, B. Hoyle, E. M. Huff, D. Huterer, B. Jain, M. Jarvis, T. Kacprzak, D. Kirk, N. Kokron, C. Krawiec, O. Lahav, A. R. Liddle, J. Peacock, M. M. Rau, A. Refregier, R. P. Rollins, E. Rozo, E. S. Rykoff, C. Sánchez, I. Sevilla-Noarbe, E. Sheldon, A. Stebbins, T. N. Varga, P. Vielzeuf, M. Wang, R. H. Wechsler, B. Yanny, T. M. C. Abbott, F. B. Abdalla, S. Allam, J. Annis, K. Bechtol, A. Benoit-Lévy, E. Bertin, D. Brooks, E. Buckley-Geer, D. L. Burke, A. Carnero Rosell, M. Carrasco Kind, J. Carretero, F. J. Castander, M. Crocce, C. E. Cunha, C. B. D'Andrea, L. N. da Costa, D. L. DePoy, S. Desai, H. T. Diehl, J. P. Dietrich, P. Doel, E. Fernandez, B. Flaugher, P. Fosalba, J. García-Bellido, E. Gaztanaga, D. W. Gerdes, T. Giannantonio, D. A. Goldstein,

R. A. Gruendl, J. Gschwend, G. Gutierrez, D. J. James, T. Jeltema, M. W. G. Johnson, M. D. Johnson, S. Kent, K. Kuehn, S. Kuhlmann, N. Kuropatkin, T. S. Li, M. Lima, H. Lin, M. A. G. Maia, M. March, J. L. Marshall, P. Martini, P. Melchior, F. Menanteau, R. Miquel, J. J. Mohr, E. Neilsen, R. C. Nichol, B. Nord, D. Petravick, A. A. Plazas, A. K. Romer, A. Roodman, M. Sako, E. Sanchez, V. Scarpine, R. Schindler, M. Schubnell, M. Smith, R. C. Smith, M. Soares-Santos, F. Sobreira, E. Suchyta, M. E. C. Swanson, G. Tarle, D. Thomas, D. L. Tucker, V. Vikram, A. R. Walker, J. Weller, and Y. Zhang. Dark Energy Survey Year 1 Results: Cosmological Constraints from Cosmic Shear. *ArXiv e-prints*, August 2017.

J. Zuntz, E. Sheldon, S. Samuroff, M. A. Troxel, M. Jarvis, N. MacCrann, D. Gruen, J. Prat, C. Sánchez, A. Choi, S. L. Bridle, G. M. Bernstein, S. Dodelson, A. Drlica-Wagner, Y. Fang, R. A. Gruendl, B. Hoyle, E. M. Huff, B. Jain, D. Kirk, T. Kacprzak, C. Krawiec, A. A. Plazas, R. P. Rollins, E. S. Rykoff, I. Sevilla-Noarbe, B. Soergel, T. N. Varga, T. M. C. Abbott, F. B. Abdalla, S. Allam, J. Annis, K. Bechtol, A. Benoit-Lévy, E. Bertin, E. Buckley-Geer, D. L. Burke, A. Carnero Rosell, M. Carrasco Kind, J. Carretero, F. J. Castander, M. Crocce, C. E. Cunha, C. B. D'Andrea, L. N. da Costa, C. Davis, S. Desai, H. T. Diehl, J. P. Dietrich, P. Doel, T. F. Eifler, J. Estrada, A. E. Evrard, A. Fausti Neto, E. Fernandez, B. Flaugher, P. Fosalba, J. Frieman, J. García-Bellido, E. Gaztanaga, D. W. Gerdes, T. Giannantonio, J. Gschwend, G. Gutierrez, W. G. Hartley, K. Honscheid, D. J. James, T. Jeltema, M. W. G. Johnson, M. D. Johnson, K. Kuehn, S. Kuhlmann, N. Kuropatkin, O. Lahav, T. S. Li, M. Lima, M. A. G. Maia, M. March, P. Martini, P. Melchior, F. Menanteau, C. J. Miller, R. Miquel, J. J. Mohr, E. Neilsen, R. C. Nichol, R. L. C. Ogando, N. Roe, A. K. Romer, A. Roodman, E. Sanchez, V. Scarpine, R. Schindler, M. Schubnell, M. Smith, R. C. Smith, M. Soares-Santos, F. Sobreira, E. Suchyta, M. E. C. Swanson, G. Tarle, D. Thomas, D. L. Tucker, V. Vikram, A. R. Walker, R. H. Wechsler, and Y. Zhang. Dark Energy Survey Year 1 Results: Weak Lensing Shape Catalogues. *ArXiv e-prints*, August 2017.